

M2S-RoAD: Multi-Modal Semantic Segmentation for Road Damage Using Camera and LiDAR Data

Tzu-Yun Tseng¹, Hongyu Lyu¹, Josephine Li², Julie Stephany Berrio¹,
Mao Shan¹, Stewart Worrall¹

¹Australian Centre for Robotics (ACFR), The University of Sydney, Australia *

² University of Washington, United States of America

¹ {t.tseng, h.lyu, j.berrio, m.shan, s.worrall}@acfr.usyd.edu.au, ² josli@uw.edu

Abstract

Road damage can create safety and comfort challenges for both human drivers and autonomous vehicles (AVs). This damage is particularly prevalent in rural areas due to less frequent surveying and maintenance of roads. Automated detection of pavement deterioration can be used as an input to AVs and driver assistance systems to improve road safety. Current research in this field has predominantly focused on urban environments driven largely by public datasets, while rural areas have received significantly less attention. This paper introduces M2S-RoAD, a dataset for the semantic segmentation of different classes of road damage. M2S-RoAD was collected in various towns across New South Wales, Australia, and labelled for semantic segmentation to identify nine distinct types of road damage. This dataset will be released upon the acceptance of the paper.

1 Introduction

Advancements in vehicular technology and artificial intelligence (AI) have led to different use cases where AI is applied to assist drivers or as a module in highly automated vehicles (AVs). This applies to scene understanding, that uses perception sensors like cameras and/or LiDARs to infer the context to the driving environments [Berrio et al., 2021]. Machine learning, a subset of AI, has proven to reach an impressive level of accuracy at perception tasks. Nevertheless, it requires large amounts of data to train models capable of interpreting

*This research is funded by Transport for New South Wales (TfNSW), iMOVE Australia and supported by the Cooperative Research Centres program, an Australian Government initiative. This research was partially supported by the Australian Government through the Australian Research Council’s ARC Training Centre funding scheme for Automated Vehicles in Rural and Remote Regions (project IC230100001).



(a) Rural road with uneven surface



(b) Rural road with potholes filled with water

Figure 1: Scenes from rural regions with road damage.

the environment around the vehicle [Minaee et al., 2022]. While there are many publicly available datasets, they are primarily focused on urban environments.

One of the objectives of scene understanding is to warn the driver or system when a hazard is detected on the road. Road damage represents a safety risk for all users [Shen et al., 2015], and local councils may be held liable if an accident occurs. Thus, significant efforts have been made to detect and repair road damage in metropolitan areas [Maeda et al., 2018], but rural regions still lack the infrastructure to quickly address issues such as the ones shown in Fig. 1.

For urban road damage detection, image-based methods are widely used as camera images offer detailed, colour-rich information about the road surface [Cao et al., 2020]. However, camera-only methods are vulnerable to lighting and weather variations, which can significantly impact the accuracy of road damage segmentation. Recently, 3D information, such as disparity maps [Li and Liu, 2021] or LiDAR point clouds [Meivel

et al., 2024], has been incorporated to address this issue. Integrating depth data into these methods has proven to enhance the robustness of road anomaly detection [Caltagirone et al., 2019].

For road damage detection, there is a lack in publicly available datasets that include LiDAR point clouds, making it challenging to evaluate and improve methodologies proposed in the literature [Chang et al.,]. Due to this, it is also difficult to innovate and create new methods for identifying road damage.

This proposed dataset aims to address the gaps in existing datasets for road damage, particularly the under-representation of rural environments and the absence of datasets that include LiDAR point clouds. The M2D-RoAD dataset provides camera images, LiDAR point clouds, and sensor calibration, enabling research on multi-modal segmentation of road damage.

The contributions of this paper are listed as follow:

- M2S-RoAD is the first dataset for semantic segmentation of road damage collected under different weather and illumination conditions in several cities and road scenes. The annotations cover 9 types of road damage.
- M2S-RoAD is the first multi-modal dataset to fuse polygon-labelled images with corresponding point clouds to accurately understand the shape and depth of the road damage.
- Benchmark evaluation and analysis on five different image-based semantic segmentation techniques as a baseline for comparisons on new methods.

2 Related Datasets

Multiple datasets have been developed for detecting road surface damage, with most relying on single images, and some incorporating stereo vision to estimate depth as shown in Table 1. Image-based approaches to object identification generally fall into two categories: detection using 2D bounding boxes and pixel-level semantic segmentation. This section reviews the datasets available in the literature, focusing on the sensors used and the types of annotations provided.

2.1 RGB Image-Based Datasets

The two main types of annotations used in RGB image-based datasets are pixel-wise semantic labels and 2D bounding boxes.

Pixel-Level Annotated Datasets

Cracktree206 Dataset: Cracktree206 [Zou et al., 2012] provides 206 images of road surfaces captured using an area-array camera. The dataset includes pixel-level annotations and augmented images. Each image contains manually annotated ground-truth crack curves.

CCSAD Dataset: The CCSAD dataset [Guzmán et al., 2015] was collected in Mexico with 500 GB of stereo images, videos, and metadata. The dataset is divided into four parts: Colonial Town Streets, Urban Streets, Avenues, and Small Roads and Tunnel Networks. It provides depth and stereo data which are highly affected by lighting and shadow conditions.

CrackForest Dataset: The CrackForest dataset [Shi et al., 2016] consists of 118 high-resolution images of cracks took by iPhone 5 in urban Beijing. Each image has been resized to 480×320 pixels for uniformity with pixel-wise annotations.

CRACK500 Dataset: CRACK500 [Zhang et al., 2016] is aiming specifically to detect crack. Composed of 1,896 training images, 328 validation images, and 1,124 test images, and each image is further divided into smaller cropped parts to increase the dataset size. Pixel-wise annotations by multiple annotators are provided for cracks.

Deepcrack Dataset: The DeepCrack dataset [Liu et al., 2019] consists of 537 RGB colour images with manually annotated segments. Each image has a resolution of 544 × 384 pixels. The dataset is divided into two subsets: a training set with 300 images and a testing set with 237 images. Pixel-level annotations are provided

NHA12D Dataset: The NHA12D dataset [Huang et al., 2022] includes 80 images of concrete and asphalt pavements, collected by vehicles on the A12 network in the UK. The images have a resolution of 1928×1080 and pixel-wise annotations for crack and non-crack regions. The dataset captures a variety of road features, including road markings, vehicles, water stains, road studs, and other random objects.

CQU-BPDD Dataset: The CQU-BPDD dataset [Tang et al., 2021] consists of 60,059 high-resolution asphalt road images (1200×900 pixels), collected in southern China using in-vehicle cameras. Also provided with patch-level annotations for seven types of pavement damage, including transverse cracks, longitudinal cracks, alligator cracks, crack pouring, raveling, repairs, and normal conditions. The CQU-BPDD dataset captures 2×3 meter pavement patches, each image regarded as a candidate box for binary image classification.

EdmCrack1000 Dataset: EdmCrack1000 [Mei et al., 2020] contains 1000 images, each with a resolution of 1920×1080 pixels for detecting cracks. The camera is installed outside and rear of the car to avoid interference from windows or the windshield.

Bounding-Box Annotated Datasets

RDD2018 Dataset: The RDD2018 dataset [Maeda et al., 2018] contains 9,053 road images (600 × 600 pixels) captured across seven Japanese cities, with 15,435 annotated bounding boxes. It spans a range of weather and lighting with the bounding boxes annotation with smart-

Table 1: Comparison of road damage datasets. Pixel-wise label (PL) datasets often fall into the binary classification (BC) category to differentiate between crack and background. As for datasets with bounding-box (BB) label, even though they are Multi Class (MC) they are not as accurate as compared to those with PL-based labels.

Dataset	Camera	Label	Resolution	Size	Location	Features	Class
Cracktree206	Area-array	PL	800×600	206 images	N/A	Augmented by rotation and flipping	BC
CCSAD	scA1300-32fm	PL	1096×822	500 GB	Mexico	Lighting, reflection, and shadow	MC
CrackForest	iPhone 5	PL	480×320	118 images	Beijing	Urban road cracks	BC
CRACK500	Smartphone	PL	Varied	3.3k images	Multiple	Dataset divided into cropped parts	BC
Malillary Vistas	Varied	PL, IL	1920×1080	25k images	Worldwide	World-wide coverage	MC
Deepcrack	Line-array	PL	544×384	537 images	N/A	Asphalt and concrete road	BC
NHA12D	Camera	PL	1920×1080	80 images	UK	Concrete and asphalt pavements	BC
CQU-BPDD	Vehicle-mounted	Patch-level	1200×900	60k images	China	Candidate box	BC
EdmCrack1000	Vehicle-mounted	PL	1920×1080	1k images	Canada	Shadows and occlusions	BC
RDD2018	Smartphone	BB	600×600	9k images	Japan	Eight types of damage	MC
RDD2019	Smartphone	BB	128×128	13.1k images	Japan	Night types of damage	MC
GAPs	Monochrome	BB	1920×1080	2k grayscale images	Germany	Patch size 64×64	MC
RDD2020	Smartphone	BB	600×600 to 720×720	26.3k images	India, Japan, Czech Republic	Diverse road conditions	MC
RDD2022	Smartphone, drone, motor-bike	BB	512×512 to 3650×2044	47.4k images	6 countries	Expanded RDD2020 to 3 more countries	MC
SHREC 2022	RGB-D	PL	Varied	4.3k image/mask pairs, 797 video clips	Multiple	Potholes and cracks	BC
Pothole-600	ZED Stereo	PL	Varied	67 stereo image pairs	N/A	Disparity transform	MC
Sunny	GoPro	N/A	3680×2760	48.9k images	N/A	Image processing	N/A
M2S-RoAD	Vehicle-mounted	PL	1928×1208	1071 images and 43911 point clouds	NSW, Australia	Different weather and illumination conditions	MC

phone shoot 10m ahead.

RDD2019 Dataset: RDD2019 [Maeda et al., 2021] further enrich the RDD2018 with utility hole as a new class and resize into 128X128 pixels. RDD2019 datasets consists of 13,135 images augmented by GAN and 30,989 annotated bounding boxes but shared the same coverage as RDD2018 in Japan.

German Asphalt Pavement Distress (GAPs) Dataset: The GAPs dataset [Eisenbach et al., 2017] consists of 1,969 gray-scale images with bounding-box annotations for various types of road damage, including cracks, potholes, inlaid patches, applied patches and open joints. Each image has a resolution of 192 × 1080 pixels. The dataset is divided into 1,418 training images, 51 validation images, 500 validation-test images and 500 test images. Annotations are by bounding boxes containing detailed damage categories.

RDD2020 Dataset: RDD2020 [Arya et al., 2020] expand the coverage to the Czech Republic and India to enrich the datasets with 26,336 images. It contains 4 different damage type instances, such as potholes, longitudinal cracks, alligator cracks and lateral cracks, total round to 25,046 instances with two resolutions 600×600 and 720×720 respectively.

RDD2022 Dataset: The RDD2022 dataset [Arya

et al., 2022] is the most extensive version of the RDD series, with 47,420 images and 55,007 bounding box annotations. The coverage expands to six different countries with the image captured by different sensors including smartphone, camera and google street view from vehicles, drones and motorbikes. The image resolutions varies from 512×512, 600×600 and 720×720 to 3650×2044.

2.2 Depth Sensor-Based Datasets

Sunny Dataset: The Sunny dataset [Nienaber et al., 2015] consists of 48,913 high-resolution images (3680×2760 pixels) captured with a GoPro camera mounted in a vehicle. Depth information is provided through stereo matching but does not specify about the labels, as this dataset comes up with image processing rather than machine learning.

SHREC 2022 Dataset: The SHREC 2022 RGB-D dataset [Thompson et al., 2022] includes 4,340 pixel-wise image/mask pairs and 797 unannotated RGB-D video clips, with depth and disparity maps for just pothole and crack detection. The resolution is 1920×1080 for RGB-D video and is 640×400 for disparity videos at grayscale, as disparity images help to detect road damage.

Pothole-600 Dataset: Pothole-600 [Fan et al., 2019]

consists of 67 pairs of stereo images captured using a ZED stereo camera. The dataset provides depth information through disparity maps and the resolutions for different subsets are 1028×1730 , 1030×1720 and 1028×1710 .

CyberPothole Dataset: This synthetic dataset [KC et al., 2024] for pothole detection provides depth maps with 2D bounding boxes annotations. The data was created using templates based on real-world images and rendering the potholes in blender to simulate the depth maps.

This paper presents M2S-RoAD, the first dataset with semantic segmentation labels and corresponding point clouds annotated on 9 types of road damage. The data was collected with a front-facing camera (1928×1208 resolution) and one LiDAR (128 beams). The data logging occurred in rural regions across different weather, illumination, cities, and road types.

3 The M2S-RoAD Dataset

Data collection, post-processing, and annotating the images for semantic segments containing road damage is required to create this comprehensive dataset. This dataset is necessary for training and validating a computer vision system able to detect and classify road damage in diverse and representative environmental conditions. This section outlines the entire process, from sensor setup to creating the final labelled dataset.

3.1 Platform

We employed two synchronised sensors for data collection: a front-facing camera and a LiDAR, both mounted on an vehicle (Volkswagen Passat). The SF3324 automotive GMSL model’s camera is integrated with an ONSEMI CMOS Image Sensor AR0231 (2M pixels) and a SEKONIX ultra-high-resolution lens. This configuration offers a horizontal field of view (FOV) of 120 degrees and a vertical FOV of 73 degrees, capturing images at a resolution of 1928×1208 pixels (2.3M pixels) [Lyu et al., 2025]. The LiDAR sensor is an Ouster OS1-128 mounted on the roof. It provides 360-degree 3D data coverage and enables the real-time reconstruction of depth images, signal images, and ambient images of the driving environment. The OS1-128 features a vertical resolution of 128 beams within a 45-degree vertical FOV and a maximum range of 120 meters.

As illustrated in Fig. 2, the camera and LiDAR were mounted horizontally and centrally on the data collection platform at heights of 1.47 meters and 1.84 meters above the ground, respectively.

Calibration

The camera calibration process estimates the lens and image parameters, which enables the correction of lens

distortion, accurate measurement of object sizes, and calculation of the camera’s position within the scene. Intrinsic calibration is performed using the fisheye camera model [Kannala and Brandt, 2006], with parameters including focal length, principal points, and four fisheye equidistant distortion coefficients. For this calibration, we use the ROS image pipeline [Mihelich and Bowman, 2024]. The process involves positioning a checkerboard (calibration target) across the entire field of view at close range and in various orientations. An optimisation algorithm is then employed to calculate the camera and image parameters.

Extrinsic sensor calibration specifies the spatial relationship between the camera and LiDAR, allowing for integrating data from multiple sensors into a unified coordinate frame. For this purpose, we employed our lidar-camera calibration package [Verma et al., 2019] [Tsai et al., 2021] to calculate the transformation matrix between the camera and LiDAR frames. These transformations are represented as a 6-degree-of-freedom (6-DOF) pose, encompassing $[x, y, z]$ coordinates and $[\text{roll}, \text{pitch}, \text{yaw}]$ angles.

Fig. 3 shows each point in the LiDAR point cloud overlaid onto the corresponding location in the camera’s image, mapping the 3D data from the LiDAR onto the camera’s 2D image plane. The colours of the points depict the distance from the camera to the objects in the scene. Red indicates points that are close to the camera, while blue points are farther away. This process allows for the fusion of data from both sensors.

Data Collection

The data was logged while driving across various towns in New South Wales, Australia, including Cudal, Katoomba, Lithgow, and Bathurst. We selected these places to capture a different environmental conditions. The data was collected under varying weather and illumination conditions, including sunny, cloudy, rainy, and overcast conditions.

The images in Fig. 4 showcase road surface conditions across different regions of New South Wales under varying weather conditions. The first image depicts a wet road in Cudal during rainy weather, highlighting the presence of puddles in a rural setting. The second image shows a narrow road in Katoomba under overcast skies, with dry yet shaded conditions. The third image captures a railway crossing on a sunny day, where the road surface is well-lit and dry. Finally, the fourth image presents an urban road intersection in Bathurst during cloudy weather, with visible road markings and dry pavement.

Using data taken from a large variety of weather conditions was important due to the way the weather affected the presentation of anomalies. For instance, the depth of

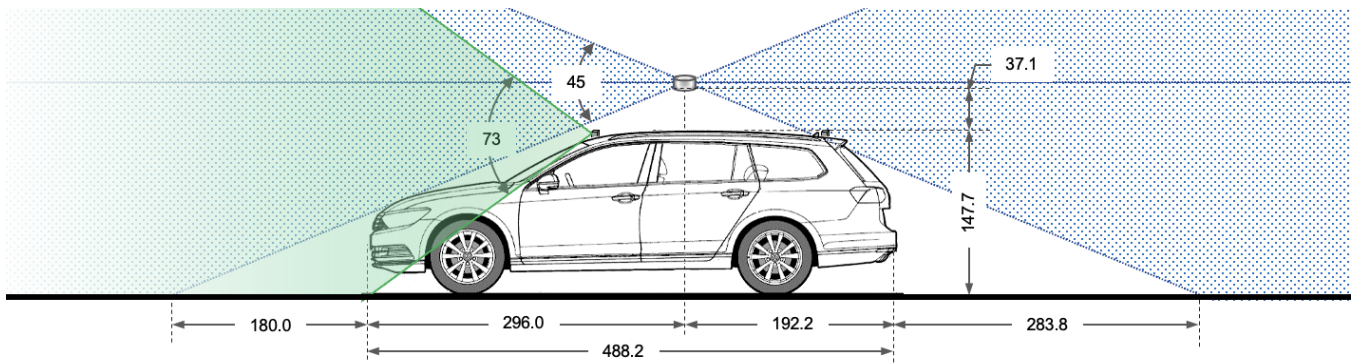


Figure 2: Sensor configuration of the data collection platform equipped with a 360-degree LiDAR and a front-facing camera.

a pothole looks very different under sunny weather versus overcast skies; additionally, certain categories such as “pothole with water” would only show up under certain weather conditions. It was also necessary to take into consideration the variation in visibility caused by abnormal weather conditions; for example, in heavy rain or extremely sunny weather, the ability of the camera to accurately capture the surroundings is decreased.

Image Selection

Images were selected to provide a wide variety of examples in terms of various types of road damage as well as across different weather and road conditions. Footage was first selected to encompass different kinds of environments and weather. However, as the images were taken as frames from the video and our original pool comprised of thousands of images, many of the images did not have any road damage, or did not have the categories of damage that we are looking to highlight. The final set of images to be annotated were chosen based



(a) Road surface at a road crossing during sunny weather



(b) Road surface in Bathurst during cloudy weather



(c) Road surface in Cudal during rainy weather



(d) Road surface in Katoomba during overcast weather

Figure 4: Road surface conditions in various regions of New South Wales under different weather conditions.

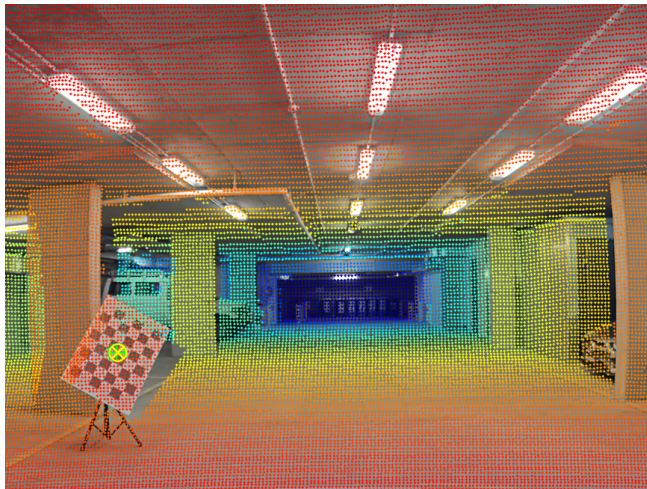


Figure 3: LiDAR point cloud projected onto the camera image using the camera’s intrinsic parameters and the extrinsic calibration between the camera and LiDAR.

on how much value they could contribute to the resulting dataset. We selected images that were spread out throughout the videos and showed anomalies in a range of different environments, such as in different positions on the road, having different degrees of severity, or under varying levels of visibility. Furthermore, a conscious effort was made to balance the amount of images that showcased each category of damages; images that contained significantly more common categories were sometimes passed over in order to minimise the difference between the number of images in each category.

All of the images were categorised into four subsets to reflect the weather conditions during data collection. The subsets include: *Sunny*, *Cloudy*, *Rainy* and *Overcast*

conditions.

Since the camera and LiDAR are synchronised, we use the camera-image timestamp to extract 20 preceding and 20 following LiDAR point clouds (captured at a rate of 10 Hz). This approach allows us to combine the point clouds, creating a denser 3D representation that simplifies the annotation in the 3D domain. With the intrinsic calibration of the camera and its known position relative to the LiDAR, it is possible to project the annotations from the image onto the LiDAR points.

Anonymisation

The images were anonymised to ensure compliance with local regulations. This involved a thorough process where identifiable elements, such as number plates and faces, were identified and manually blurred to prevent potential privacy breaches. It was ensured that these elements were blurred beyond recognition and readability, and were double-checked to confirm. The anonymisation process was carried out to maintain the integrity of the visual data while adhering to legal and ethical protocols.

Annotation

We used the LabelMe [Wada, 2018] tool to annotate the images by outlining the road damage with polygons. The labels for the M2S-RoAD dataset capture nine key road damage, chosen for relevance to rural driving environments:

Pothole: Potholes are bowl-shaped depressions in the road surface, usually round or oval in shape. They are characterised by rough, jagged edges that are often surrounded by loose debris. Potholes can range from shallow to deep and are common on a variety of road surfaces, including asphalt, dirt, and grass.

Potholes with Water: Potholes appear very differently when filled with water, as reflections off the water distort camera and LiDAR readings; thus, potholes with water were classified separately than ordinary potholes. Water-filled potholes pose a hazard because the water masks the true depth and boundaries of the depression, making it difficult to accurately assess the hazard.

Cracks: Cracks are fractures in the pavement that appear as distinct lines either longitudinally or transversely. Cracks are typically narrower than slippage and may form around areas where potholes have been patched. Cracks appear both independently and in clusters, spanning large portions of the road.

Corrugation: Also known as washboards, corrugations consist of a series of closely spaced ridges and valleys created in the road surface. This effect is common on unpaved roads, especially those made of dirt or gravel, and is caused by repeated traffic.

Rutting: Rutting are longitudinal depressions formed along wheel paths of roads, caused by the repeated passage of heavy vehicles. Over time, road materials com-

press under the pressure of traffic, forming grooves that can lead to unsafe driving conditions. It is most recognisable by the width of the tracks, matching the wheel width of cars.

Slippage: Slippage defects appear as wide, crescent-shaped cracks or areas where the top layer of pavement slips or separates from the underlying layers. Slippage is often seen at intersections or areas that experience frequent turning, sometimes including the shoulder or side of the road. Slipping is an early indicator of potential pavement failure and often occurs on ageing or poorly maintained asphalt roads.

Drain: Drain covers themselves can pose a hazard in the road, and more pertinently, the road around or along a drain typically involves some kind of angle or channel to guide the water. These areas or channels are important for vehicles to recognise as they stray from the expected uniformity of the road and after rainy weather can also be prime locations for hydroplaning.

Bump: Bumps are raised areas in the pavement that can be caused by frost heave, underlying root growth, or construction defects, as well as intentional additions such as speed bumps. Bumps vary in size but can be differentiated from corrugation by frequency and compactness.

Manhole: Manholes are covered openings in the road, typically designed for maintenance use and providing access to underground. Additionally, poorly cared for manholes can mirror larger bumps or potholes in the road, and the road around manholes is particularly susceptible to more extreme damage.

Point Cloud Projection

Labelling road damage in the point cloud domain is not a straightforward process. We leverage the image annotations and sensor calibration to map the labels onto the point cloud data.

Using the individual scans corresponding to the labelled images, we calculate the position of the LiDAR for each scan. To achieve this, we use KISS-ICP [Vizzo et al., 2023] to calculate these positions in space. We then concatenate all the LiDAR scans to build a denser point cloud. We project the points onto the image using the camera’s intrinsic parameters and the extrinsic calibration between the two sensors.

Once the 3D points are mapped to the image frame, we retrieve labels for the points that fall within the annotated polygons and assign these labels to the corresponding 3D points. Fig. 5 depicts the outcome of this process, with the right image displaying the annotated image and the left figure showing the projection of the labels onto the point cloud. The code for this transformation is available at <https://github.com/chinitaberrio/M2S-RoAD>.

3.2 Dataset Statistics

The Fig. 6 depicts the distribution of road damage labels in the M2S-RoAD dataset and its subsets. The dataset subsets are categorised based on weather conditions with an additional category labelled “full”, which represents the combined distribution across all weather conditions.

Cracks are the most dominant label across the dataset, the ‘drain’ label also shows a large presence in the *sunny* subset. Pothole with water represents almost 60% of the annotations for the *rainy* dataset. Other damage types, such as potholes, slippage, manholes, bumps, and corrugations, are less common, which indicates their relative scarcity in the dataset.

4 Semantic Segmentation Experiments

In this section, we present semantic segmentation experiments on the M2S-RoAD dataset. We outline the task setup, evaluation metrics, and baseline methods. These methods were evaluated on the full validation set and subsets for four weather conditions, categorising results into five colour-coded sections. Finally, we discuss and analyse the outcomes to assess their performance.

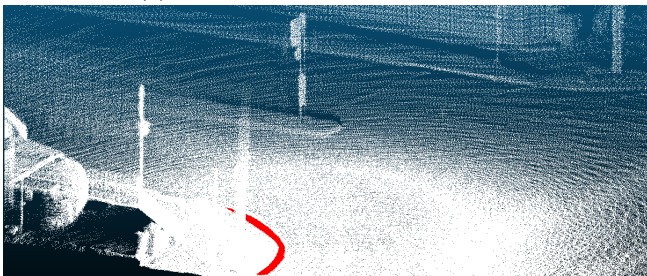
Task and Metrics

Semantic segmentation aims to classify every pixel in an image, or each point in point clouds, enabling detailed 2D or 3D scene understanding. We utilise images with a resolution of 1928×1208 to generate segmentation maps that categorise nine types of road damage, including potholes, cracks, slippage, rutting, and manhole.

To assess a semantic segmentation model, we employ the mean Intersection over Union (mIoU) metric, sometimes referred as the mean Jaccard Index. This metric



(a) Image with slippage annotation



(b) Slippage label transferred to the point cloud

Figure 5: Label transfer from image to point cloud domain.

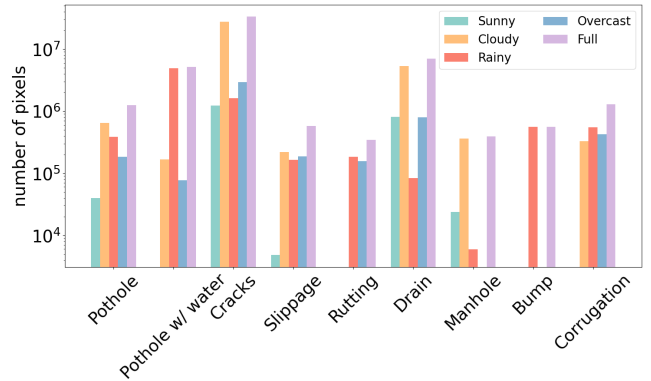


Figure 6: Distribution of annotated pixels (y-axis) across each class (x-axis) in the M2S-RoAD dataset and its subsets.

averages the Intersection over Union (IoU) [Everingham et al., 2015] across all classes:

$$\text{IoU}_i = \frac{TP_i}{TP_i + FP_i + FN_i}$$

$$\text{mIoU} = \frac{1}{N} \sum_{i=1}^N \text{IoU}_i$$

where TP_i , FP_i , and FN_i denote the number of true positives, false positives, respectively, and false negatives for class i , and N represents the total number of classes.

Baseline Approaches

We assessed five state-of-the-art semantic segmentation techniques on the M2S-RoAD dataset: ISANet [Huang et al., 2019], BiSeNetV2 [Yu et al., 2021], STDC [Fan et al., 2021], SegFormer [Xie et al., 2021], and Mask2Former [Cheng et al., 2022].

The BiSeNet series [Yu et al., 2018, Yu et al., 2021] employs a dual-branch network architecture with a guided aggregation layer to integrate features from both branches. However, the additional stream reduces the computational efficiency. In order to solve this problem, STDC [Fan et al., 2021] proposes a short-term dense connection network that extracts image features with multi-scale information and expandable receptive fields. It incorporates spatial context into the low-level details, enhancing performance without lengthening the inference time.

ISANet [Huang et al., 2019] enhances efficiency by employing Interleaved Sparse Self-Attention (ISSA). ISSA divides the dense similarity matrix into two sparse matrices. Built upon ResNet [He et al., 2016], ISANet uses ISSA to generate segmentation outputs that align with the spatial dimensions of the input image.

Latest progress in semantic segmentation have been driven by transformer-based techniques. A frame-

Table 2: **Semantic segmentation results on the M2S-RoAD validation set and its subsets.** The results are organised by weather conditions: Blue indicates the *sunny* subset (first section), Yellow represents the *cloudy* subset (second section), Gray shows the *rainy* subset (third section), and Red corresponds to the *overcast* subset (fourth section). Green highlights results for the entire validation set (fifth section). The evaluated methods include ISANet [Huang et al., 2019], BiSeNetV2 [Yu et al., 2021], STDC [Fan et al., 2021], SegFormer [Xie et al., 2021], and Mask2Former [Cheng et al., 2022]. A hyphen (-) indicates unavailable or inapplicable data.

Method	mIoU	pothole	pothole w/ water	cracks	slippage	rutting	drain	manhole	bump	corrugation
BiSeNetV2	36.65	0.43	-	89.58	0.0	-	93.23	0.0	-	-
STDC	60.87	21.35	-	91.14	0.0	-	91.84	100.0	-	-
ISANet	71.49	70.20	-	93.41	0.0	-	93.82	100.0	-	-
SegFormer	65.72	45.9	-	91.87	0.0	-	90.83	100.0	-	-
Mask2Former	59.08	40.27	-	81.62	0.0	-	73.7	99.79	-	-
BiSeNetV2	45.87	12.08	32.21	95.8	0.0	-	87.42	47.7	-	-
STDC	68.93	49.61	54.39	96.44	46.12	-	87.97	79.05	-	-
ISANet	80.88	56.62	63.59	96.91	99.96	-	89.2	79.0	-	-
SegFormer	62.39	51.64	63.4	97.39	60.05	-	90.74	73.53	-	-
Mask2Former	67.33	41.93	62.93	96.13	32.7	-	93.26	77.03	-	-
BiSeNetV2	20.99	15.12	74.55	31.79	0.0	0.0	-	-	0.0	25.48
STDC	52.71	16.47	91.12	45.84	21.37	44.99	-	-	97.88	51.31
ISANet	50.75	12.96	87.37	39.32	22.87	48.02	-	-	96.33	48.4
SegFormer	53.23	15.02	86.59	47.87	23.73	45.97	-	-	97.49	55.96
Mask2Former	49.36	24.68	84.72	30.95	21.03	45.03	-	-	96.82	42.3
BiSeNetV2	53.64	41.74	55.83	84.14	0.0	-	89.69	-	-	50.44
STDC	64.23	72.16	75.4	89.15	5.19	-	96.87	-	-	46.6
ISANet	60.86	77.9	53.89	89.71	0.0	-	95.28	-	-	48.37
SegFormer	66.50	62.2	57.49	93.05	17.82	-	97.73	-	-	70.73
Mask2Former	74.92	58.22	69.51	89.77	75.48	-	93.04	-	-	63.47
BiSeNetV2	38.65	15.76	73.26	89.99	0.0	0.0	87.64	43.24	0.0	37.97
STDC	65.26	36.31	89.1	93.39	20.66	33.0	89.57	77.02	97.9	50.4
ISANet	65.47	33.47	85.86	93.09	26.17	36.68	90.14	80.03	95.97	47.82
SegFormer	67.06	33.48	85.62	94.0	26.65	34.79	91.38	74.74	97.49	65.41
Mask2Former	67.77	33.5	83.45	91.45	37.25	44.23	90.97	78.14	96.81	54.12

work called SegFormer [Xie et al., 2021] integrates multi-layer perceptrons (MLP) with transformers. The MLP decoder then combines multi-scale features to create representations for producing segmentation maps. Mask2Former [Cheng et al., 2022] introduces a Masked-attention Mask Transformer for semantic segmentation. Its decoder improves feature encoding and speeds up converging by concentrating on anticipated mask regions through masked attention.

We adapted the implementation of baseline methods from the MMSegmentation library for training and evaluation on the M2S-RoAD dataset. BiSeNetV2 [Yu et al., 2021] was trained from scratch, while the backbones of the other four methods were initialised with ImageNet-1K [Deng et al., 2009] pre-trained weights.

Results and Discussion

Table 2 shows semantic segmentation results for the M2S-RoAD dataset, highlighting performance differences across four weather conditions and the nine road damage types. The methods achieve their best overall average performance of 65.08% on the *cloudy* subset, while their lowest performance is 45.41% on the *rainy*

subset. The reason for this difference is that cloudy weather provides ample light and visibility, along with 34 million labelled pixels for diverse training samples. In contrast, rainy conditions face image quality challenge, like, lens fogging, raindrops, and reflections.

The performance of the baseline methods is closely linked to the representativeness of road damage types in the dataset. For instance, when segmenting cracks and rutting, the models achieve average performances of 92.38% and 29.74%, respectively. This disparity arises because cracks account for 66.67% of labelled pixels, making them the most representative samples, while rutting represents only 0.69%. This imbalance enables effective feature learning for cracks but limits support for rutting, ultimately impacting overall performance.

The weather-specific categories show significantly better performance on relevant weather subsets. For example, when segmenting potholes with water, the baseline methods achieve an average performance of 84.87% in the *rainy* subset, compared to just 55.30% and 62.42% in the *cloudy* and *overcast* subsets, respectively. This disparity likely stems from the fact that potholes with water primarily occur in rainy conditions, making up 58.11% of labelled pixels in the *rainy* subset, while representing less than 2% in the other two subsets.

Transformer-based methods outperform CNN-based approaches in road damage segmentation. Mask2Former achieves the highest performance at 67.77%, while BiSeNetV2 has the lowest performance at only 38.65%. This gap is largely due to the larger parameter count in Transformers and their global self-attention mechanism, which better captures features and details of different road damage.

5 Conclusion

This paper introduces a new dataset for semantic segmentation of diverse road surface damage types, and illustrates the diverse environmental and weather-related challenges faced by road surfaces in New South Wales, Australia.

From the experiment analysis, we discovered that some classes need more images to be labelled. In the future, we will focus on expanding the dataset to make it more balanced and improve the performance of machine learning methods.

Although we successfully transferred the labels from the image to the point cloud, we will evaluate the semantic segmentation task for 3D points in the future.

This work serves as the starting point for multi-modal segmentation of road damage. We aim to develop a method combining lidar and camera data to detect and segment road damage.

References

- [Arya et al., 2020] Arya, D., Maeda, H., Ghosh, S. K., Toshniwal, D., Omata, H., Kashiyama, T., and Sekimoto, Y. (2020). Global road damage detection: State-of-the-art solutions. In *2020 IEEE International Conference on Big Data (Big Data)*, pages 5533–5539. IEEE.
- [Arya et al., 2022] Arya, D., Maeda, H., Ghosh, S. K., Toshniwal, D., and Sekimoto, Y. (2022). Rdd2022: A multi-national image dataset for automatic road damage detection. *Geoscience Data Journal*.
- [Berrio et al., 2021] Berrio, J. S., Shan, M., Worrall, S., and Nebot, E. (2021). Camera-lidar integration: Probabilistic sensor fusion for semantic mapping. *IEEE Transactions on Intelligent Transportation Systems*, 23(7):7637–7652.
- [Caltagirone et al., 2019] Caltagirone, L., Bellone, M., Svensson, L., and Wahde, M. (2019). Lidar-camera fusion for road detection using fully convolutional neural networks. *Robotics and Autonomous Systems*, 111:125–131.
- [Cao et al., 2020] Cao, M.-T., Tran, Q.-V., Nguyen, N.-M., and Chang, K.-T. (2020). Survey on performance of deep learning models for detecting road damages using multiple dashcam image resources. *Advanced Engineering Informatics*, 46:101182.
- [Chang et al.,] Chang, K. T., Chang, J. R., and Liu, J. K. *Detection of Pavement Distresses Using 3D Laser Scanning Technology*, pages 1–11.
- [Cheng et al., 2022] Cheng, B., Misra, I., Schwing, A. G., Kirillov, A., and Girdhar, R. (2022). Masked-attention mask transformer for universal image segmentation. In *Proceedings of the IEEE/CVF conference on computer vision and pattern recognition*, pages 1290–1299.
- [Deng et al., 2009] Deng, J., Dong, W., Socher, R., Li, L.-J., Li, K., and Fei-Fei, L. (2009). Imagenet: A large-scale hierarchical image database. In *2009 IEEE conference on computer vision and pattern recognition*, pages 248–255. Ieee.
- [Eisenbach et al., 2017] Eisenbach, M., Stricker, R., Seichter, D., Amende, K., Debes, K., Sesselmann, M., Ebersbach, D., Stoeckert, U., and Gross, H.-M. (2017). How to get pavement distress detection ready for deep learning? a systematic approach. In *2017 international joint conference on neural networks (IJCNN)*, pages 2039–2047. IEEE.
- [Everingham et al., 2015] Everingham, M., Eslami, S. A., Van Gool, L., Williams, C. K., Winn, J., and Zisserman, A. (2015). The pascal visual object classes challenge: A retrospective. *International journal of computer vision*, 111:98–136.
- [Fan et al., 2021] Fan, M., Lai, S., Huang, J., Wei, X., Chai, Z., Luo, J., and Wei, X. (2021). Rethinking bisenet for real-time semantic segmentation. In *Proceedings of the IEEE/CVF conference on computer vision and pattern recognition*, pages 9716–9725.
- [Fan et al., 2019] Fan, R., Ozgunalp, U., Hosking, B., Liu, M., and Pitas, I. (2019). Pothole detection based on disparity transformation and road surface modeling. *IEEE Transactions on Image Processing*, 29:897–908.
- [Guzmán et al., 2015] Guzmán, R., Hayet, J.-B., and Klette, R. (2015). Towards ubiquitous autonomous driving: The ccsad dataset. In *Computer Analysis of Images and Patterns: 16th International Conference, CAIP 2015, Valletta, Malta, September 2-4, 2015 Proceedings, Part I 16*, pages 582–593. Springer.
- [He et al., 2016] He, K., Zhang, X., Ren, S., and Sun, J. (2016). Deep residual learning for image recognition. In *Proceedings of the IEEE conference on computer vision and pattern recognition*, pages 770–778.
- [Huang et al., 2019] Huang, L., Yuan, Y., Guo, J., Zhang, C., Chen, X., and Wang, J. (2019). Interlaced sparse self-attention for semantic segmentation. *arXiv preprint arXiv:1907.12273*.
- [Huang et al., 2022] Huang, Z., Chen, W., Al-Tabbaa, A., and Brilakis, I. (2022). Nha12d: A new pavement crack dataset and a comparison study of crack detection algorithms. *arXiv preprint arXiv:2205.01198*.
- [Kannala and Brandt, 2006] Kannala, J. and Brandt, S. S. (2006). A generic camera model and calibration method for conventional, wide-angle, and fish-eye lenses. *IEEE Transactions on Pattern Analysis and Machine Intelligence*, 28(8):1335–1340.
- [KC et al., 2024] KC, K., Berrio, J. S., Worrall, S., and Balamurali, M. (2024). Cyberpotholes: Pothole defect detection using synthetic depth-maps. In *2024 IEEE Intelligent Transportation Systems Conference (ITSC)*.
- [Li and Liu, 2021] Li, R. and Liu, C. (2021). Road damage evaluation via stereo camera and deep learning neural network. In *2021 IEEE Aerospace Conference (50100)*, pages 1–7. IEEE.
- [Liu et al., 2019] Liu, Y., Yao, J., Lu, X., Xie, R., and Li, L. (2019). Deepcrack: A deep hierarchical feature learning architecture for crack segmentation. *Neurocomputing*, 338:139–153.
- [Lyu et al., 2025] Lyu, H., Berrio, J. S., Shan, M., and Worrall, S. (2025). Sydneyscapes: Image segmen-

- tation for australian environments. *arXiv preprint arXiv:2504.07542*.
- [Maeda et al., 2021] Maeda, H., Kashiyama, T., Sekimoto, Y., Seto, T., and Omata, H. (2021). Generative adversarial network for road damage detection. *Computer-Aided Civil and Infrastructure Engineering*, 36(1):47–60.
- [Maeda et al., 2018] Maeda, H., Sekimoto, Y., Seto, T., Kashiyama, T., and Omata, H. (2018). Road damage detection and classification using deep neural networks with smartphone images. *Computer-Aided Civil and Infrastructure Engineering*, 33(12):1127–1141.
- [Mei et al., 2020] Mei, Q., Gül, M., and Azim, M. R. (2020). Densely connected deep neural network considering connectivity of pixels for automatic crack detection. *Automation in Construction*, 110:103018.
- [Meivel et al., 2024] Meivel, S., Devi, K. I., Subramanian, A. S., and Kalaiarasi, G. (2024). Remote sensing analysis of the lidar drone mapping system for detecting damages to buildings, roads, and bridges using the faster cnn method. *Journal of the Indian Society of Remote Sensing*, pages 1–17.
- [Mihelich and Bowman, 2024] Mihelich, P. and Bowman, J. (2024). Image pipeline. https://github.com/ros-perception/image_pipeline. Accessed: 2024-09-04.
- [Minaee et al., 2022] Minaee, S., Boykov, Y., Porikli, F., Plaza, A., Kehtarnavaz, N., and Terzopoulos, D. (2022). Image segmentation using deep learning: A survey. *IEEE Transactions on Pattern Analysis and Machine Intelligence*, 44(7):3523–3542.
- [Nienaber et al., 2015] Nienaber, S., Booyesen, M. J., and Kroon, R. (2015). Detecting potholes using simple image processing techniques and real-world footage.
- [Shen et al., 2015] Shen, Y., Hermans, E., Bao, Q., Brijs, T., and Wets, G. (2015). Serious injuries: an additional indicator to fatalities for road safety benchmarking. *Traffic injury prevention*, 16(3):246–253.
- [Shi et al., 2016] Shi, Y., Cui, L., Qi, Z., Meng, F., and Chen, Z. (2016). Automatic road crack detection using random structured forests. *IEEE Transactions on Intelligent Transportation Systems*, 17(12):3434–3445.
- [Tang et al., 2021] Tang, W., Huang, S., Zhao, Q., Li, R., and Huangfu, L. (2021). An iteratively optimized patch label inference network for automatic pavement distress detection. *IEEE Transactions on Intelligent Transportation Systems*, 23(7):8652–8661.
- [Thompson et al., 2022] Thompson, E. M., Ranieri, A., Biasotti, S., Chicchon, M., Sipiran, I., Pham, M.-K., Nguyen-Ho, T.-L., Nguyen, H.-D., and Tran, M.-T. (2022). Shrec 2022: Pothole and crack detection in the road pavement using images and rgb-d data. *Computers & Graphics*, 107:161–171.
- [Tsai et al., 2021] Tsai, D., Worrall, S., Shan, M., Lohr, A., and Nebot, E. (2021). Optimising the selection of samples for robust lidar camera calibration. In *2021 IEEE International Intelligent Transportation Systems Conference (ITSC)*, pages 2631–2638.
- [Verma et al., 2019] Verma, S., Berrio, J. S., Worrall, S., and Nebot, E. (2019). Automatic extrinsic calibration between a camera and a 3d lidar using 3d point and plane correspondences. In *2019 IEEE Intelligent Transportation Systems Conference (ITSC)*, pages 3906–3912.
- [Vizzo et al., 2023] Vizzo, I., Guadagnino, T., Mersch, B., Wiesmann, L., Behley, J., and Stachniss, C. (2023). KISS-ICP: In Defense of Point-to-Point ICP – Simple, Accurate, and Robust Registration If Done the Right Way. *IEEE Robotics and Automation Letters (RA-L)*, 8(2):1029–1036.
- [Wada, 2018] Wada, K. (2018). Labelme: Image polygonal annotation with python.
- [Xie et al., 2021] Xie, E., Wang, W., Yu, Z., Anandkumar, A., Alvarez, J. M., and Luo, P. (2021). Segformer: Simple and efficient design for semantic segmentation with transformers. *Advances in neural information processing systems*, 34:12077–12090.
- [Yu et al., 2021] Yu, C., Gao, C., Wang, J., Yu, G., Shen, C., and Sang, N. (2021). Bisenet v2: Bilateral network with guided aggregation for real-time semantic segmentation. *International journal of computer vision*, 129:3051–3068.
- [Yu et al., 2018] Yu, C., Wang, J., Peng, C., Gao, C., Yu, G., and Sang, N. (2018). Bisenet: Bilateral segmentation network for real-time semantic segmentation. In *Proceedings of the European conference on computer vision (ECCV)*, pages 325–341.
- [Zhang et al., 2016] Zhang, L., Yang, F., Zhang, Y. D., and Zhu, Y. J. (2016). Road crack detection using deep convolutional neural network. In *2016 IEEE international conference on image processing (ICIP)*, pages 3708–3712. IEEE.
- [Zou et al., 2012] Zou, Q., Cao, Y., Li, Q., Mao, Q., and Wang, S. (2012). Cracktree: Automatic crack detection from pavement images. *Pattern Recognition Letters*, 33(3):227–238.